THE JOURNAL OF PHYSICAL CHEMISTRY C

pubs.acs.org/JPCC Article

Effect of TiO_x Substrate Interactions on the Electrocatalytic Oxygen Reduction Reaction at Au Nanoparticles

Aigerim Galyamova,[$] Kihyun Shin,[$] Graeme Henkelman,[*] and Richard M. Crooks[*]

Cite This: J. Phys. Chem. C 2020, 124, 10045−10056 Read Online

ACCESS | Metrics & More | Article Recommendations | Supporting Information

ABSTRACT: In this article, we report a robust model for studying electrocatalytic reactions at metal nanoparticles (NPs) in contact with metal oxide surfaces. The metal oxide layer (TiO_x) is prepared by atomic layer deposition, and it is sufficiently thin that it does not hinder electron transfer from the underlying conductive electrode to the supported AuNP electrocatalysts. In advance of the experiments, density functional theory (DFT) predicted that direct contact between AuNPs and TiO_x would lead to enhanced activity for the oxygen reduction reaction (ORR). DFT attributes the observed ORR enhancement to partial charge transfer from oxygen vacancies within the TiO_x film to the supported AuNPs and hence formation of anionic Au species. The experimental findings are in near quantitative agreement with the DFT results. Specifically, compared to isolated AuNPs, decreases of ∼100 and ∼50 mV in the ORR onset potential are observed experimentally for AuNPs supported on $TiO_{1.9}$ and $TiO_{2.0}$ films, respectively.

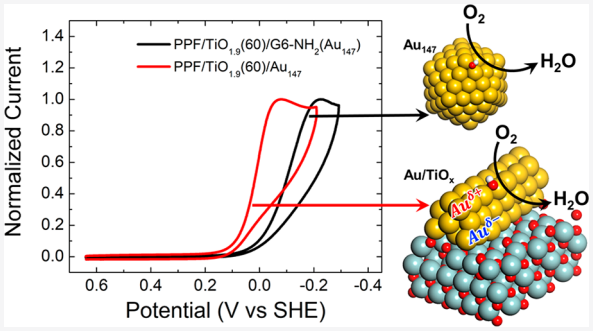

INTRODUCTION

In this work, we report on a synergistic relationship between Au nanoparticles (NPs) and TiO_x (x = 1.9 and 2.0) supports that leads to significantly improved electrocatalytic activity for the oxygen reduction reaction (ORR) compared to AuNPs in the absence of a support effect. Importantly, the electrocatalyst was selected by theoretical screening of different supports prior to the initiation of the experiments. Additionally, the findings discussed here build upon an earlier study from our groups in which density functional theory (DFT) was used to predict the nature of a different metal/support combination that would be beneficial for the ORR. The present study was undertaken to determine if the general principles that led to quantitative agreement between predictive theory and confirming experiments in this earlier work were fortuitous or if the approach used is robust. The results presented here suggest the latter.

As alluded to above, we previously reported a model that allowed us to study the effects of support interactions on the electrocatalytic response of metal NPs in the absence and presence of direct contact with metal oxide substrates.[1−4] In this model (Scheme 1), dendrimer encapsulated NPs (DENs)[5−8] are used as the principal catalyst.

Initially, the dendrimer prevents direct contact between the NPs and the underlying metal oxide support, and therefore electrocatalytic activity arises only from the metal NPs. Subsequent removal of the dendrimer by a UV/O_3 treatment brings the NPs into direct contact with the oxide. Depending on the nature of the oxide, it might influence the electrocatalytic properties of the NPs. For example, we have shown that alumina substrates have no effect on the oxygen reduction activity of PtNPs.[1,2] In contrast, SnO_x substrates significantly influence AuNPs for the same reaction.[3] Calculations, carried out prior to these latter experiments, predicted that this activity enhancement would exist due to a partial charge transfer from oxygen vacancies in the SnO_x support to the AuNPs. Furthermore, we have shown that the presence of the dendrimer around the NP has little to no effect on ORR activity.[3,4]

In addition to the aforementioned results from our group, Adzic and co-workers have also examined the effect of oxide supports on electrocatalytic reactions.[9−11] For example, they

Scheme 1

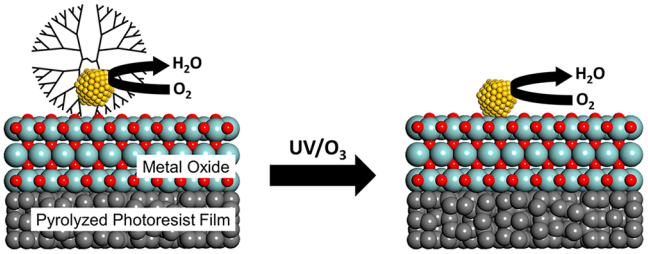

Received: March 28, 2020
Revised: April 13, 2020
Published: April 28, 2020

https://dx.doi.org/10.1021/acs.jpcc.0c02754
J. Phys. Chem. C 2020, 124, 10045−10056

investigated the role of support interactions for the ethanol oxidation reaction at a SnO_x/Pt interface.[9] This interface was fabricated by depositing SnO_x nanoislands onto a Pt(111) surface, and it resulted in enhanced ethanol electrooxidation compared to Pt alone. The degree of activity enhancement was found to be highly dependent on SnO_x coverage, which clearly implicated the symbiotic relationship between SnO_x and Pt. In this case, SnO_x nanoislands were concluded to be actively promoting the removal of poisoning species, such as Co_{ads}, from the Pt surface.

In a related study, Wang and co-workers investigated the ORR at PdNPs supported on TiO_2 monosheets with and without oxygen vacancies present.[12] The results showed that in the presence of oxygen vacancies, there was a small improvement in the onset potential for the ORR compared to commercially available carbon-supported PtNP catalysts. Interestingly, PdNPs supported on TiO_2 having oxygen vacancies were found to be significantly more active for the ORR than when the vacancies were absent. As in our SnO_x study,[3] the enhancement was attributed to charge transfer from oxygen vacancies present in TiO_2 to PdNPs.

We began the present study by performing DFT calculations to identify possible synergy between AuNP catalysts and a rutile TiO_2(110) support. The calculations were carried out on isolated Au_{147} NPs, naked rutile TiO_2(110), and an Au nanorod supported on TiO_2(110). Reaction pathways were investigated by calculating the binding energy of reactants, products, and any intermediates. The predicted overpotential for the ORR was determined by the voltage required to make each elementary step exoergic. These calculations indicate that charge transfer between Au and TiO_2(110) influences the activity of the Au nanorod and lowers the ORR overpotential by ∼100 mV compared to unsupported AuNPs.

To evaluate the accuracy of the foregoing DFT calculations experimentally, we deposited ∼2.8 nm-thick TiO_x films (x = 1.9 and 2.0), using atomic layer deposition (ALD), over pyrolyzed photoresist films (PPF).[13] Next, Au DENs composed of an average of 147 atoms (Au_{147}) were immobilized onto this support. This construct (left side of Scheme 1) was evaluated for the ORR, and then the dendrimer was removed (right side of Scheme 1). As discussed earlier, this places the Au_{147} NPs into direct contact with the TiO_x support. In the latter case, a positive shift in the ORR onset potential of ∼100 mV is observed. Surface analysis by X-ray photoelectron spectroscopy (XPS) revealed the presence of increased electron density on the Au_{147} NPs when they are in direct contact with the TiO_x support. According to the DFT calculations, this accounts for the enhanced ORR activity.

EXPERIMENTAL SECTION

Computational Methods. GGA-level, spin-polarized DFT calculations were performed with the Vienna ab initio simulation package (VASP) using a plane wave basis set with a cutoff energy of 400 eV. The Perdew−Wang (PW91) functional was used to describe electron exchange and correlation.[14] The DFT+U method was employed to treat localized Ti 3d orbitals with an effective U value of 4 eV, as reported in previous papers.[15,16] The Brillouin zone was sampled at the γ point, which was found to be sufficient given the large system size. The convergence criteria for electronic and geometric optimization were 10^{-5} eV and 0.01 eV/Å, respectively.

Unsupported Au_{147} NPs were modeled as both icosahedral (Ih) and cuboctahedral (COh) structures. A TiO_2(110) slab and a Au nanorod supported on the TiO_2(110) slab (TiO_2(110)/Au) were also modeled to determine if there are any synergistic effects between the Au nanocatalyst and the metal oxide support that might improve ORR activity. These atomic models are illustrated in Figure S1. The supported Au was modeled as a nanorod instead of an Au_{147} cluster to both capture the TiO_2(110)/Au interface and to minimize the computational cost. The Au_{147} NPs were isolated with a 10 Å vacuum gap in all directions, and all atoms were relaxed during the geometric optimization process. Both the TiO_2(110) and the TiO_2(110)/Au systems had a 20 Å vacuum gap in the z-direction; the bottom two TiO_2 layers were fixed in their bulk positions. A surface Pourbaix diagram was calculated to identify the stable surface structures in the operating potential range of the ORR.[17] To calculate the ORR activity, the following four associative reaction steps were considered.

$$\Delta G_1: \quad O_2(g) + H^+ + e^- + * \leftrightarrow OOH^*$$

$$\Delta G_2: \quad OOH^* + H^+ + e^- \leftrightarrow O^* + H_2O(l)$$

$$\Delta G_3: \quad O^* + H^+ + e^- \leftrightarrow OH^*$$

$$\Delta G_4: \quad OH^* + H^+ + e^- \leftrightarrow H_2O(l) + *$$

The ORR overpotential was found by a reaction energy diagram, drawn with the following eq 1.[18]

$$\Delta G(U) = \Delta E + \Delta ZPE - T\Delta S + neU \tag{1}$$

where ΔE is the reaction energy, ΔZPE is the zero-point energy correction, ΔS is the change in entropy, ne is the number of electrons, and U is the applied potential. The chemical potential of the solvated proton and electron pair ($H^+ + e^-$) at standard conditions (p_{H_2} = 1 bar, a_{H^+} = 1, T = 298.15 K) is calculated as $0.5\mu^0_{H_2(g)} - eU$ by assuming equilibrium at the standard hydrogen electrode.[19,20] Solvation effects, modeled by surrounding the adsorbed species with water molecules, were included in the calculated reaction energy diagrams.[21]

Chemicals and Materials. The following chemicals were used as received: 1,1′-ferrocenedimethanol ($Fc(MeOH)_2$, 98%, Acros Organics); KNO_3 (99.994% trace metal basis, Alfa-Aesar); $AgNO_3$ (99.85%, Acros Organics); $HClO_4$ (+70%, ultrapure grade, J. T. Baker); NaOH (1 M, Fischer Scientific); $NaBH_4$ (99.99% trace metals basis, Sigma-Aldrich); gold(III) chloride trihydrate (99.9% trace metals basis, Sigma-Aldrich); and tetrakis(dimethylamino)titanium(IV) (TDMAT, 99%, STREM Chemicals, Inc.). The following compressed gases were purchased from Praxair (Austin, TX): high-purity N_2 (99.998%), high-purity O_2 (99.995%), high-purity Ar (99.998%), and forming gas (5% H_2/95% N_2).

Sixth-generation, amine-terminated, poly(amidoamine) dendrimers (G6-NH_2) were purchased as a 9 wt % methanol solution from Dendritech, Inc. (Midland, MI). For the DENs synthesis, methanol was removed from the stock solution under vacuum and the dendrimers were reconstituted in water. UHPLC-grade water from Sigma-Aldrich was used to reconstitute the dendrimers, to synthesize DENs, and to prepare all aqueous solutions.

Fused quartz slides (GE 124, 3" × 1" × 1 mm) were purchased from Technical Glass Products, Inc. (Painesville

https://dx.doi.org/10.1021/acs.jpcc.0c02754
J. Phys. Chem. C 2020, 124, 10045−10056

Twp, OH). Photoresist (AZ 1518) and photoresist developer (AZ 400 K, 1:4) were purchased from Integrated Micro Materials (Argyle, TX).

Fabrication of Pyrolyzed Photoresist Film (PPF) Electrodes. PPF electrodes were fabricated using a slightly modified version of a previously reported procedure.[3] Details can be found in the Supporting Information.

Deposition of TiO_x (x = 1.9 and 2.0) Films on PPF Electrodes. The metal oxide thin-films were deposited using a Savannah S100 Cambridge NanoTech ALD system (Ultratech, San Jose, CA). The titanium precursor, TDMAT, was heated to 75 °C, and the oxygen precursor (H_2O) was maintained at room temperature (22−25 °C). The ultrathin TiO_x films were deposited as follows. First, PPF electrodes were placed in the ALD chamber, which was then evacuated (<1 mmHg) and heated to 150 °C for 10 min under a constant N_2 flow (20 sccm). Second, the heated PPF electrodes were exposed to ten 0.015 s pulses of O_3; each O_3 pulse was followed with a 20 s purge with N_2. The purpose of this step was to introduce oxygen functionalities onto the PPF surface, thereby encouraging ALD. Third, an ALD cycle was carried as follows: (1) 0.10 s pulse of TDMAT; (2) 20.0 s purge with N_2; (3) 0.015 s pulse of H_2O; and (4) 20.0 s purge with N_2. These four steps were repeated until the desired number of cycles were completed. This procedure results in formation of TiO_x films having a Ti/O ratio of 1.0:1.9 ($TiO_{1.9}$). To obtain stochiometric $TiO_{2.0}$, the as-deposited films were further oxidized by heating in a tube furnace at 200 °C for 2 h under a constant flow of O_2 (60 sccm).

Synthesis of Au DENs. G6-NH_2(Au_{147}) DENs were synthesized using a previously published procedure.[3] Specifically, 10.0 mL of 2.0 μM G6-NH_2(Au_{147}) DENs was prepared as follows. First, 200 μL of 100 μM of an aqueous G6-NH_2 dendrimer solution was added to 8.65 mL of vigorously stirred UHPLC water. Second, 147 μL of 20.0 mM $HAuCl_4$ was pipetted dropwise into the diluted dendrimer solution. Third, within 2 min after adding the first drop of the $HAuCl_4$ solution, a ∼67-fold molar excess of $NaBH_4$ (in 1.0 mL of 0.30 M NaOH) was added. Fourth, the reaction mixture was stirred overnight in air to deactivate excess $NaBH_4$. This synthesis has previously been shown to produce one AuNP (1.7 ± 0.2 nm) per dendrimer.[22]

Prior to immobilization of the G6-NH_2(Au_{147}) DENs onto the PPF/TiO_x supports, the pH of the G6-NH_2(Au_{147}) DENs solution was adjusted to ∼3.2 using 1 M $HClO_4$. This did not change the size distribution of the AuNPs (Figure S2). The G6-NH_2(Au_{147}) DENs were immobilized by immersing the PPF/TiO_x supports in the G6-NH_2(Au_{147}) DENs solution for 90 min. After immobilization, the modified supports (PPF/TiO_x/G6-NH_2(Au_{147})) were rinsed with a gentle flow of UHPLC water, dried under a flow of Ar, and then dried in air for at least 1 h prior to the use.

UV/O_3 Method for Decomposition of G6-NH_2 Dendrimers. The procedure for decomposing the dendrimers using UV/O_3 has been previously reported.[3] The resulting PPF/TiO_x/Au_{147} modified supports were left to equilibrate with the ambient lab atmosphere for at least 45 min before use.

Structural Characterization. XPS measurements were performed using a Kratos Axis Ultra DLD spectrometer (Chestnut Ridge, NY). Samples were mounted on Cu tape and grounded with carbon tape. Spectra were collected using an Al Kα source, 0.10 eV step size, and 20 eV band-pass energy. Charge neutralization was used during collection of each spectrum. CasaXPS (version 2.3.19, Casa Software, Teignmouth, UK) was used for peak fitting and quantitative data analysis. Binding energies (BEs) were calibrated using the C 1s line of PPF (284.50 eV).[23,24] Symmetric line shapes were fitted using a mixed Gaussian/Lorentzian model, while asymmetric line shapes were fitted using an asymmetric Lorentzian model. The concentration of oxygen vacancies in the TiO_x films were calculated using the ratio of atomic concentrations of O 1s and Ti 2p signals. Specifically, the O 1 s signal was deconvoluted to obtain the fraction of oxygen bound to Ti, while the Ti 2p signal was used without additional processing. More details are provided in the Supporting Information.

Ellipsometric thickness measurements were performed using a J. A. Woollam M-2000D spectroscopic ellipsometer (Lincoln, NE). Data were collected between 45° and 65° with 5° increments and a 10 s dwell time at each step. A three-layer model was used for data analysis: the first layer was 1.0 mm of SiO_2, the second layer was 500 nm of PPF, and the third layer was amorphous TiO_x films of varying thickness. The optical constants for the materials were either provided by the manufacturer (SiO_2),[25] determined experimentally (PPF), or found in literature (TiO_2).[26]

The topography of the PPF/TiO_x thin films was determined using a Wyko NT9100 optical profilometer having a white light source and 0.1 nm vertical resolution. The data were collected using 20.0× magnification over an area of 237 μm × 316 μm.

The crystallinity of the PPF/TiO_x thin films was studied using X-ray diffraction. For these measurements, the incident beam was scanned at 2°/min with a 0.05° step size and a 2.5° Soller slit.

Transmission electron microscope (TEM) images were collected using a JEOL-2010F TEM having a point-to point resolution of 0.2 nm. A 2.0 μL portion of the G6-NH_2(Au_{147}) solution was pipetted onto a carbon-mesh-over-Cu TEM grid (Electron Microscopy Sciences, Hatfield, PA). The samples were left to dry in the laboratory ambient air for at least 5 h prior to analysis.

Scanning electron microscope (SEM) images were collected using a FEI Quanta 650 microscope with an accelerating voltage of 15 kV and a spot size of 3.0.

Electrochemical Characterization. A CHI 700D bipotentiostat and an Hg/Hg_2SO_4 reference electrode were used for all electrochemical measurements (CH Instruments Inc., Austin, TX). A Pt wire counter electrode was used for experiments in the flow cell and a glassy carbon rod counter electrode (Alfa Aesar, Tewksbury, MA) was used for all other electrochemical measurements. All potentials were converted to the standard hydrogen electrode to simplify comparison of experimental data and theoretical calculations.

The nonflow cyclic voltammetry experiments were performed in a Teflon electrochemical cell. The geometric area of the working electrode (12.4 mm^2) was defined by a Viton O-ring. The extent of passivation and the stability of the PPF/TiO_x supports were determined using a 1.0 mM $Fc(MeOH)_2$ redox probe in 0.10 M KNO_3. For these experiments, the electrode potential was scanned between 0.14 and 0.83 V at 0.010 V/s.

Prior to ORR experiments, the PPF/TiO_x/G6-NH_2(Au_{147}) or PPF/TiO_x/Au_{147} modified supports were electrochemically cleaned in an Ar-saturated, 0.10 M $HClO_4$ solution. During cleaning, the electrode potential was scanned ten times between 0.44 and 1.51 V at 0.050 V/s. Following electro-

https://dx.doi.org/10.1021/acs.jpcc.0c02754
J. Phys. Chem. C 2020, 124, 10045−10056

chemical cleaning, ORR measurements were performed in an O_2-saturated, 0.10 M $HClO_4$ solution. For these experiments, the electrode potential was scanned between 0.64 and −0.29 V at 0.050 V/s. For the nonflow electrocatalytic measurements a glassy carbon rod counter electrode was used to avoid Pt contamination of the working electrode surface.

The kinetic measurements and the product-distribution experiments were performed using a flow cell and linear sweep voltammetry. The design and the characteristics of the flow cell have been previously reported.[2] Briefly, the flow cell has the following dimensions. The gap between the generator electrode (GE) and the collector electrode (CE) ranges from 10.1 to 11.5 mm, depending on the length of the quartz substrate on which the GE is patterned. The GE and CE lengths are 100 μm and 7.6 mm, respectively, and the channel width is 500 μm. For each surface modification, the electrocatalytic measurements were performed at volumetric flow rates of 10, 15, 20, 25, and 30 μL/min. The system was allowed to equilibrate between each flow rate change for 10 min.

RESULTS AND DISCUSSION

Theoretical ORR Activity on Au_{147}. Before discussing the TiO_2(110)/Au integrated system, we first consider the isolated Au_{147} NPs and the rutile TiO_2(110) surface to identify the ORR activity of each of the individual components. For the Au_{147} NPs, Ih and COh structures were considered, which are known to be stable for NPs having sizes on the order of 1−2 nm. Calculations of the relative energy of these two structures indicate that Ih is more stable than COh by 2.90 eV, which is in agreement with our previous combined theoretical and experimental EXAFS study of Au_{147} NPs.[27] Accordingly, the binding energies of the ORR intermediates (O*, OH*, and OOH*) were calculated for the Au_{147} Ih NPs to determine the reaction energy profiles shown in Figure 1a.

For isolated Au_{147} Ih NPs, the ORR reaction intermediates are stabilized at the edge of the NP and not on the (111) facets. Figure 1a shows the most stable binding sites for each intermediate. For the ORR rate-determining step, ΔG_4, the edge sites have an overpotential of η = 0.87 V. This means a strong OH* binding energy inhibits formation of H_2O. Following a review of ORR catalysts, we can construct a volcano plot with ΔG_4 and ΔG_1 using the OH* binding energy as the descriptor.[28,29] On this volcano plot, Pt is positioned on the left side of the peak, indicating that a strong OH* binding energy on Pt limits its ORR activity.[28] Specific to our case, Au_{147} Ih NP has a stronger OH* binding energy than Pt by 0.47 eV, and therefore, it is necessary to reduce the OH* binding energy to increase the ORR activity. The COh structure was also considered for the ORR, and an even higher overpotential (Figure S3, η = 1.06 V,) was found compared to that of Au_{147} Ih (η = 0.87 V). In summary, the Ih structure is both more stable and has a higher predicted activity than COh; we therefore use the Ih structure for subsequent modeling.

ORR Activity on TiO_2(110). Calculations similar to those performed for the Au_{147} NPs were carried out for a rutile TiO_2(110) slab, and we found that the ORR intermediates bind strongly on the Ti atoms. Indeed, as shown in Figure 1b, rutile TiO_2(110) exhibits low ORR activity and a high overpotential: η = 1.37 V, which is higher than that of isolated Au_{147} NPs. Specifically, a weak O* binding energy results in ΔG_2 becoming rate determining for the ORR on the rutile TiO_2(110) slab. We conclude that the ORR is not likely to proceed on TiO_2 within the experimentally relevant potential window.

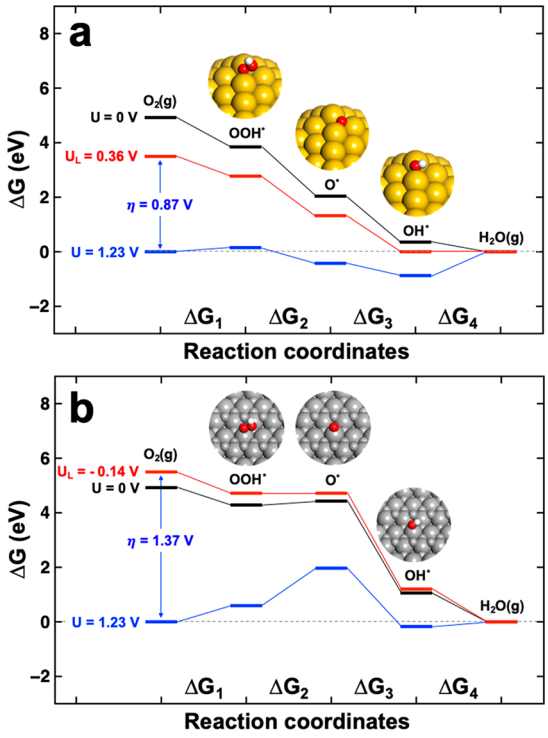

Figure 1. Gibbs free energy diagrams for the ORR pathway and overpotential (η) for (a) Au_{147} Ih NP and (b) rutile TiO_2(110). η = 1.23 − limiting potential (U_L).

Surface Pourbaix Diagram of TiO_2(110)/Au. Under actual ORR operating conditions there are additional factors affecting the electrocatalytic activity of the TiO_2(110)/Au system including the applied potential and concentration of O_2. Accordingly, we calculated the surface Pourbaix diagram for this system to determine the most energetically favorable surface configuration for ORR activity. Specifically, oxygen coverages from 30% (with a structure labeled as 3O) to 90% (9O) and oxygen vacancy concentrations from 1 to 3 ($1O_{vac}$, $2O_{vac}$, and $3O_{vac}$, respectively), were considered. Each of these surface configurations (as shown in Figure S4) are stable within specific potential windows. In the case of oxygen vacancies, the $3O_{vac}$ structure is stable at potentials lower than −0.24 V and $2O_{vac}$ is stable in a potential range of −0.24 to −0.04 V. In contrast, the stoichiometric TiO_2(110)/Au surface is stable in a lower potential range (−0.17 to 0.33 V). In the case of oxygen surface coverage, the 4O structure is stable in an intermediate potential range (0.33 to 0.83 V) and the 7O structure is stable at potentials above 0.83 V. Accordingly, we conclude that the stoichiometric TiO_2(110)/Au surface is the most stable configuration under the experimental ORR conditions.

As we discuss later, the ORR will commence at ∼0.01 V on the PPF/TiO_x/G6-NH_2(Au_{147}) modified supports. As shown in Figure S4, the most stable configuration at the potentials used in the experimental portion of this study is the stoichiometric TiO_2(110)/Au surface. Nevertheless, later in the discussion we also consider the effect the oxygen vacancies on the ORR activity.

ORR Activity on Stoichiometric TiO_2(110)/Au. In the previous section, we showed that stoichiometric TiO_2(110)/

https://dx.doi.org/10.1021/acs.jpcc.0c02754
J. Phys. Chem. C 2020, 124, 10045−10056

Au is stable under ORR operating conditions. We now focus on how the ORR activity changes when a Au nanorod is supported on the $TiO_2(110)$ surface. To elucidate possible synergistic effects of the supported $TiO_2(110)$/Au system, two reaction sites are considered: (1) on top of the Au nanorod (top site) and (2) an interface site between the Au nanorod and the $TiO_2(110)$ support.

Figure 2 shows Gibbs free energy diagrams for the ORR pathway and overpotential for $TiO_2(110)$/Au at the two different reaction sites.

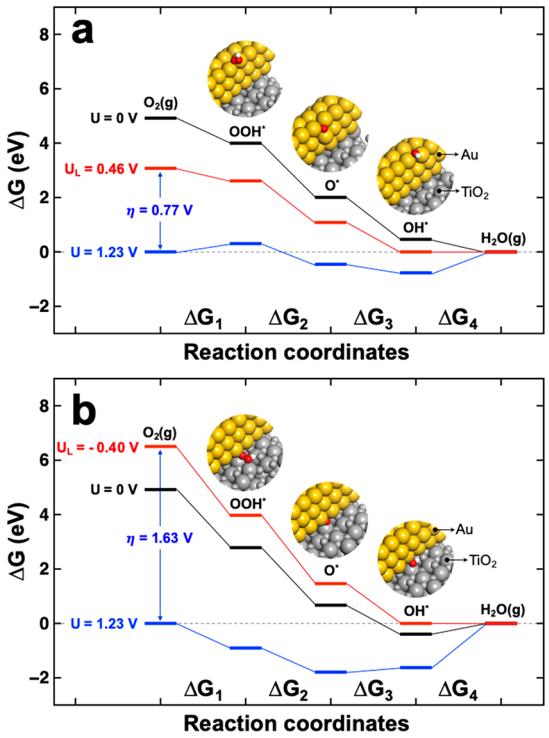

Figure 2. Gibbs free energy diagrams for the ORR pathway and overpotential (η) for $TiO_2(110)$/Au at different reaction sites (a) on the Au nanorod and (b) at the interface between Au and TiO_2.

Specifically, Figure 2a applies to the top site and Figure 2b to the interface site. For the top site, all ORR intermediates were adsorbed onto the top edge of the Au nanorod, which has a similar binding site to that of the Au_{147} Ih NP. Our calculations show that the binding energies are similar to those on the Au_{147} Ih NPs, with the OH* binding energy being slightly weaker. For the interface site, all ORR intermediates bind between a Au atom in the bottom layer of the nanorod and a Ti atom with five neighboring oxygen atoms on the top layer of the TiO_2 slab. The binding geometries are illustrated in Figure 2.

Our findings reveal that in the unsupported NP core, the Au atoms are slightly oxidized (average charge of -0.05 e$^-$), but they become more reduced (to $+0.03$ e$^-$) at the NP surface. The supported Au nanorod, however, exhibits a more complicated behavior. In this case, the first layer of the Au nanorod (closest to the $TiO_2(110)$ surface) has, on average, fewer electrons (-0.07 e$^-$) than the unsupported Au nanorod. The other Au layers did not show a significant change. Looking more closely, however, the charge state of individual Au atoms on the TiO_2 surface vary significantly depending on their position. Specifically, Au atoms atop surface oxygens are significantly oxidized (-0.20 e$^-$), but Au atoms atop Ti are reduced ($+0.10$ e$^-$).

When OH* binds at a Au top site of a nanorod, those Au atoms are slightly oxidized (-0.022 and -0.008 e$^-$). Thus, a weaker binding energy of OH* on the nanorod is due to a locally oxidized charge state compared to the unsupported Au_{147} Ih NP. The important point is that this weak OH* binding energy reduces the overpotential (η = 0.77 V) by ~100 mV compared to the unsupported Au_{147} Ih NP. In the case of the interface sites at the boundary between the Au nanorod and the $TiO_2(110)$ slab, however, the intermediate binding energies are too strong (Figure 2), and this site, therefore, exhibits a high overpotential (η = 1.63 V).

The key point is that the top of the Au nanorod is predicted to have higher catalytic activity than the interface between TiO_2 and Au due to charge transfer in the $TiO_2(110)$/Au supported catalyst system.

ORR Activity on $TiO_2(110)$/Au with Oxygen Vacancies. The $TiO_2(110)$/Au surface Pourbaix diagram (Figure S4) reveals that the presence of oxygen vacancies is unfavorable within rutile TiO_2 at experimentally relevant potentials. The experimentally synthesized amorphous TiO_2 thin-films are, however, more likely to have oxygen vacancies than the perfect rutile TiO_2 modeled in our simulation cell.[30] Furthermore, as we show later in the experimental part of the discussion, we synthesized amorphous TiO_x thin-films (Figure S5) having two distinct oxidation states: x = 1.9 and 2.0. Thus, we also considered the ORR activity of the $TiO_2(110)$/Au system having different number of oxygen vacancies (structures labeled as $1O_{vac}$, $2O_{vac}$, and $3O_{vac}$).

The top site (Figure 3) consistently exhibits higher ORR activity than the interface sites (Figure S6), regardless of the number of oxygen vacancies.

Specifically, the energy profiles in Figure 3 show that $TiO_2(110)$/Au, having $1O_{vac}$, $2O_{vac}$, and $3O_{vac}$, exhibit an enhanced ORR activity of ~60 mV, ~ 210 mV, and ~170 mV, respectively. Each of these surface configurations show similar energy profiles and the same limiting potential step (ΔG_4). This means the OH* binding energy remains a key descriptor of the ORR activity. Strong OH* binding energies remain problematic in the $TiO_2(110)$/Au system with oxygen vacancies, but they are weaker than that for the stoichiometric $TiO_2(110)$/Au system.

We performed a Bader charge analysis for the $1O_{vac}$, $2O_{vac}$, and $3O_{vac}$ structures to determine how electron transfer changes with the number of oxygen vacancies.[31−34] Both surface Ti and Au atoms (as shown in Figure S7) systematically obtain more electrons from oxygen vacancies. Even though surface Ti atoms become reduced with one or two oxygen vacancies, the Au nanorod remains in an oxidized charge state. Finally, Ti and Au atoms became reduced when $3O_{vac}$ are present at the surface of $TiO_2(110)$. A similar trend was observed in our XPS results, as discussed later.

Properties of TiO_x (x = 1.9 and 2.0) Film. We now turn our attention to experimental verification of the foregoing theoretical predictions. As discussed in the Introduction, the experimental model consists of PPF carbon electrodes coated with thin layers of $TiO_{1.9}$ or $TiO_{2.0}$ by ALD (Scheme 2, details provided in the Experimental Section and Supporting Information).

For the purposes of our electrocatalysis experiments, the thickness, uniformity, and stability of the TiO_x films are critical, and therefore, we address these points first.

https://dx.doi.org/10.1021/acs.jpcc.0c02754
J. Phys. Chem. C 2020, 124, 10045−10056

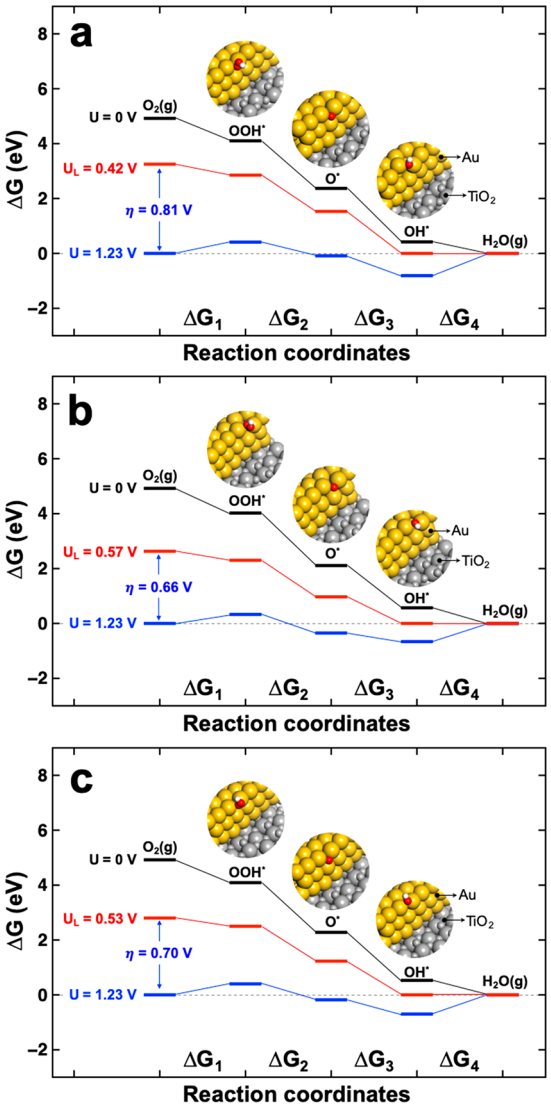

Figure 3. Gibbs free energy diagrams for TiO_2(110)/Au at Au top sites with different number of oxygen vacancies: (a) $1O_{vac}$, (b) $2O_{vac}$, and (c) $3O_{vac}$.

Scheme 2

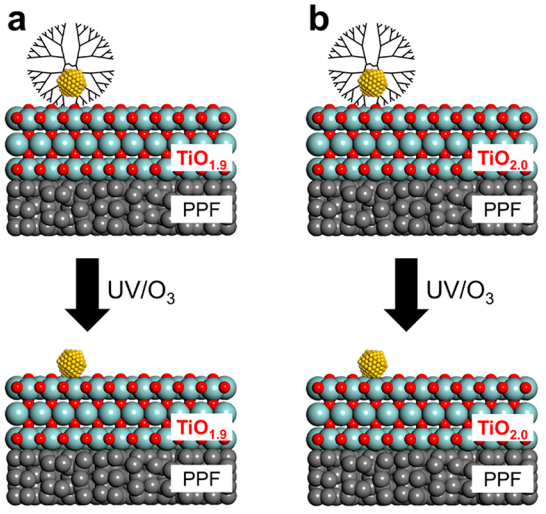

Ellipsometry was used to measure the TiO_x film thickness as a function of the number of ALD cycles performed. The resulting calibration curve (Figure S8) reveals a linear growth rate of 0.059 ± 0.002 nm/cycle with a nucleation delay of 12 ALD cycles. The nucleation delay is a well-known phenomenon in ALD in which several cycles are required before a detectable change in film thickness is observed.[35] Indeed, we have observed this behavior in our previous ALD-related studies.[1−3]

For electrocatalysis studies of the type described here, the optimal TiO_x thickness balances uniformity (no detectable pinholes) with sufficient thinness that electron transfer (eT) from PPF to the oxide-supported AuNPs is not inhibited.[36−39] As discussed next, we found this thickness to be ∼2.8 nm (equivalent to 60 ALD cycles).

Figure 4 shows cyclic voltammograms (CVs) comparing eT between PPF, PPF/$TiO_{1.9}$(60), and PPF/$TiO_{2.0}$(60) working electrodes (the number in parentheses indicates the number of ALD cycles).

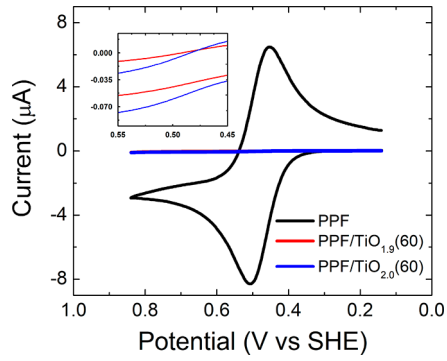

Figure 4. CVs obtained using the electrode configurations shown in the legend. The inset shows an expanded view of the voltage range over which the voltammetric peaks, if present, would be expected. The solutions contained aqueous 1.0 mM $Fc(MeOH)_2$ in 0.10 M KNO_3 and the scan rate was 0.010 V/s. The geometric area of each electrode was 12.4 mm^2. The experiments were carried out in triplicate for each surface modification.

Each CV was obtained using an aqueous solution containing 1.0 mM $Fc(MeOH)_2$ and 0.10 M KNO_3. The CV obtained using the naked PPF electrode (black) reveals well-defined oxidation and reduction peaks at 0.51 and 0.45 V, respectively. When the PPF electrode is coated with a ∼ 2.8 nm-thick $TiO_{1.9}$ layer (red), however, eT is hindered and these peaks are absent. The result is the same for the ∼2.8 nm-thick $TiO_{2.0}$-modified PPF electrode (blue, note that the blue and red lines overlap in Figure 4). These results demonstrate that the TiO_x film, regardless of its oxidation state, passivates the PPF electrode against a common molecular redox molecule.

To further confirm the absence of pinholes that might be too small or two few to be revealed by the foregoing experiment, we used a previously reported electrodeposition method.[1,40] In this experiment, we attempted to electrodeposit Ag onto the PPF/TiO_x supports. If Ag islands are observed on the surface upon subsequent examination by SEM, then the location of a latent pinhole is revealed. Electrodeposition was performed by chronoamperometry in an aqueous solution containing 0.50 mM $AgNO_3$ and 0.10 M KNO_3. The images shown in Figure S9a,b were obtained using ∼2.6 and ∼2.8 nm-thick $TiO_{1.9}$-modified PPF electrodes, respectively. The results show that

https://dx.doi.org/10.1021/acs.jpcc.0c02754
J. Phys. Chem. C 2020, 124, 10045−10056

Ag islands (e.g., pinholes) are clearly present in the ~2.6 nm-thick film, but they are absent in the ~2.8 nm-thick $TiO_{1.9}$ film. The same results is obtained for $TiO_{2.0}$-modified PPF electrodes (Figure S9c,d). We conclude that the ~2.8 nm-thick TiO_x films (60 ALD cycles) are sufficiently free of pinholes to carry out the electrocatalysis experiments described later.

The stability of ~2.8 nm-thick TiO_x films was tested under the same set of conditions used for the electrocatalysis described later. Specifically, a single PPF/TiO_x(60) support was sequentially subjected to the following conditions: immersion in a ~pH 3.0 $HClO_4$ solution for 90 min, exposure to the same UV/O_3 process that is used during dendrimer removal, and then the same series of CV scans used for the ORR study. The latter included ten electrochemical cleaning scans and three ORR scans in 0.10 M $HClO_4$ solution. The stability of the electrodes was gauged by determining their CV response to a solution containing 1.0 mM $Fc(MeOH)_2$ and 0.10 M KNO_3 (Figure S10a). The results show just a very slight increase in current for the treated electrode. Figure S10b shows analogous data for a PPF/$TiO_{2.0}$(60) electrode, and the results are the same: very little change in current. We conclude that the stability of the ~2.8 nm-thick TiO_x films under electrocatalytic conditions is sufficient for subsequent electrocatalysis studies.

Optical profilometry was used to study the topography of ~2.8 nm-thick TiO_x-modified PPF electrodes. These profilometry measurements were collected in phase-shifting mode and have a height resolution of 0.1 nm. Figure S11 shows representative topographic images over a 237 μm × 316 μm area. The average rms roughnesses of three independently prepared $TiO_{1.9}$ and $TiO_{2.0}$ films were 0.67 ± 0.06 nm and 0.60 ± 0.06 nm, respectively. These rms roughness values are in accord with other reports[41−43] as well as our own previous studies of Al_2O_3 and SnO_x films having similar thicknesses.[1,3]

The foregoing discussion demonstrates that TiO_x films deposited onto PPF electrodes have well-defined thicknesses, good topographical uniformity, and sufficient stability for electrocatalysis experiments.

Decomposition of G6-NH_2 Dendrimers. An important aspect of our approach (Scheme 1) is that the electrocatalytic properties of NPs can be evaluated in the absence or presence of support effects. However, this requires effective removal of the dendrimer. In a previous study, XPS showed that most of the organic dendrimer framework can be removed from G6-NH_2(Au_{147}) DENs immobilized onto SnO_x films using UV/O_3.[3] In the present work, we applied this same methodology to DENs immobilized onto TiO_x films.

Figure S12a shows a high-resolution XPS spectrum in the N 1s region for a PPF/$TiO_{1.9}$(60)/G6-NH_2(Au_{147}) modified support before UV/O_3 treatment. Nitrogen is a marker for the G6-NH_2 dendrimers, and the observed signal can be deconvoluted into three individual peaks corresponding to the dendrimeric amine, amide, and protonated amine functionalities.[44] Figure S12b is an XPS spectrum for the same support after UV/O_3 treatment, and it reveals an 89 ± 1% decrease in the N 1s signal. We conclude that all but ~10% of the dendrimer is removed and therefore the AuNPs reside on the $TiO_{1.9}$ surface after UV/O_3 treatment. Figure S12c,d provides analogous data for the PPF/$TiO_{2.0}$(60)/G6-NH_2(Au_{147}) surface. In this case, 78 ± 4% of the dendrimeric N is removed. Both values are in good agreement with our previous findings for dendrimer removal from SnO_x.[3]

Effect of UV/O_3 Treatment on the Oxidation States of TiO_x (x = 1.9 and 2.0) Films. According to the DFT calculations discussed earlier, oxygen vacancies (e.g., the oxidation state of TiO_x) play a crucial role in controlling the ORR activity of supported AuNPs. Because it is known that UV/O_3 can change the oxidation state of metal oxides,[3,45] we sought to determine the effect that the process of dendrimer removal exerts on the underlying oxide.

Figures S13 and S14 and Tables S1 and S2 summarize an XPS study of PPF/TiO_x electrodes before and after UV/O_3 exposure. It consists of a quantitative analysis of the Ti 2p and O 1s signals arising from the as-prepared PPF/$TiO_{1.9}$(60) film before and after UV/O_3 treatment. The results indicate that the Ti 2p/O 1s ratio remains at 1.9 even after exposure to UV/O_3. The same result is obtained for the PPF/$TiO_{2.0}$(60) film both before and after UV/O_3: the Ti 2p/O 1s ratio is 2.0 (Figure S14). We conclude, therefore, that the procedure used for decomposing the dendrimers does not measurably affect the oxidation state of the TiO_x films.

We want to emphasize that although the experimentally determined stochiometric Ti 2p/O 1s ratio after oxidation of the as-prepared $TiO_{1.9}$ films is 2.0, this value might be an overestimate due to the sensitivity limitation of XPS.[23] This means it is probably more appropriate to think of the $TiO_{1.9}$ and $TiO_{2.0}$ films as supports that have higher ($TiO_{1.9}$) and lower ($TiO_{2.0}$) concentration of oxygen vacancies.

Evaluation of ORR Onset Potential in the Absence and Presence of Interactions between AuNPs and TiO_x (x = 1.9 and 2.0) Supports. We now turn our attention to electrocatalytic results obtained using CV. These experiments were performed in an aqueous solution containing O_2-saturated, 0.10 M $HClO_4$. A glassy carbon rod counter electrode was used for these measurements to avoid Pt contamination of the electrocatalysts.

Figure 5a presents ORR CVs obtained using PPF/$TiO_{1.9}$(60)/G6-NH_2(Au_{147}) electrodes before (black) and after (red) removal of the dendrimer.

The results show that the onset of ORR activity, defined as the potential at which 10% of maximum ORR current is observed, occurs at 0.01 ± 0.01 V and 0.11 ± 0.01 V on PPF/$TiO_{1.9}$(60)/G6-NH_2(Au_{147}) and PPF/$TiO_{1.9}$(60)/Au_{147} supports, respectively. This means there is a positive shift of 100 ± 10 mV in the ORR onset potential when the AuNPs are in direct contact with a ~ 2.8 nm-thick $TiO_{1.9}$ film compared to when they are fully encapsulated within the dendrimer. Clearly, there is a favorable interaction between the AuNPs when they are in contact with underlying $TiO_{1.9}$ support. Figure 5b provides analogous results for the PPF/$TiO_{2.0}$(60)/G6-NH_2(Au_{147})-coated electrode. In this case, the positive shift is smaller, 50 ± 10 mV, but it is still unambiguous.

Importantly, the experimentally observed ~100 mV (higher O_{vac} concentration, $TiO_{1.9}$) and ~50 mV (lower O_{vac} concentration, $TiO_{2.0}$) shifts when the AuNPs are in direct with the TiO_x supports are in good agreement with DFT calculations. Recall that the corresponding DFT-predicted shifts were ~170 mV and ~60 mV for TiO_2(110)/Au having $3O_{vac}$ and $1O_{vac}$, respectively. The deviation between the experimental and theoretical results at higher oxygen vacancies concentration (100 vs 170 mV, respectively) may originate from differences between the simulation cell and the experimental model. Nevertheless, both experimental and theoretical results result in a higher degree of ORR activity when the TiO_x and AuNPs are in intimate contact. This

https://dx.doi.org/10.1021/acs.jpcc.0c02754
J. Phys. Chem. C 2020, 124, 10045−10056

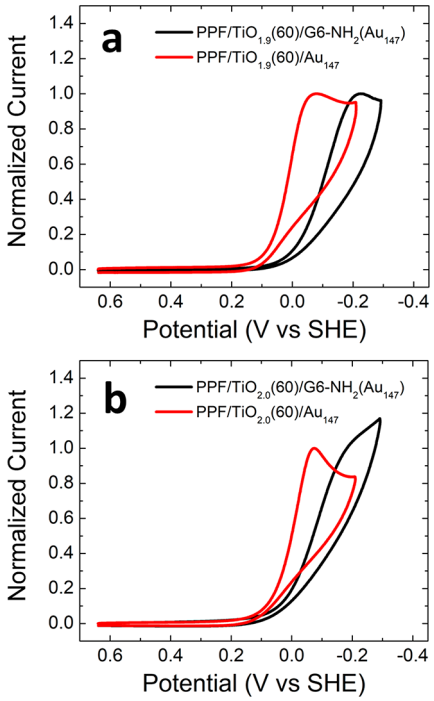

Figure 5. CVs obtained for the ORR using electrode with (a) $TiO_{1.9}$ and (b) $TiO_{2.0}$ ALD surfaces. The specific electrode modifications are given in the legends. The solutions contained aqueous, O_2-saturated 0.10 M $HClO_4$. A glassy carbon rod counter electrode was used to avoid contamination of the electrode surface. The scan rate was 0.050 V/s. The geometric area of each electrode was 12.4 mm^2. The electrodes were electrochemically cleaned prior to each ORR experiment. The onset potential was defined as that potential corresponding to 10% of the ORR peak current. The currents for each CV were normalized to the corresponding ORR peak current. The experiments were carried out in triplicate for each electrode configuration.

indicates that the magnitude of charge transfer from oxygen vacancies in TiO_x to AuNPs plays a crucial role in the increase of ORR activity. This conclusion is confirmed by XPS results discussed later.

We carried out a few key control experiments to further confirm our conclusions. For example, no ORR activity is observed on PPF/$TiO_{1.9}$(60) (Figure S15, blue trace) or PPF/$TiO_{2.0}$(60) (Figure S16, blue trace) supports when AuNPs are absent in the system. This observation is consistent with the previously discussed theoretical model that predicted a high ORR overpotential (Figure 1b, η = 1.37 V) for the TiO_2 film alone (no AuNPs). Note, however, that the TiO_x films are active for the hydrogen evolution reaction at potentials higher than −0.20 V (Figures S15 and S16).[46] This activity affects the shape of ORR CVs on PPF/TiO_x/G6-NH_2(Au_{147}) at high negative potentials. Consequently, the ORR current does not decay monotonically after reaching diffusion-limited conditions.

We carried out a second control experiment in which the ORR was investigated in the absence and presence of contact between AuNPs and the PPF electrode (no TiO_x). These experiments were carried out exactly as described earlier for the case when the TiO_x support was present. PPF is a carbon electrode that is not known to affect electrocatalytic activity of supported metal NPs, and therefore, we expected that the ORR onset potential would be the same before and after dendrimer removal.[47] The results in Figure S17 and Table S3 confirm this hypothesis.

The key conclusion of the ORR CV experiments is that there are shifts of ∼100 mV and ∼50 mV toward lower potentials when AuNPs are in direct contact with $TiO_{1.9}$ and $TiO_{2.0}$ supports, respectively. The control experiments cited above clearly implicate direct contact between the AuNPs and TiO_x as the cause of this shift. Finally, the experimental results are in rather good agreement with the DFT predictions.

Evaluation of ORR Pathway in Absence and Presence of Interactions between AuNPs and TiO_x (x = 1.9 and 2.0) Support. In addition to the CV results, we also determined the number of electrons (n_{eff}) transferred during the ORR for each of the electrocatalysts. These experiments were carried out using a custom-designed flow cell that we have described previously.[2] The principal virtue of the reported flow cell is that the working electrode can be easily removed and subsequently replaced. This flexibility makes it possible to obtain microelectrochemical measurements on exactly the same electrode before and after dendrimer removal, and to quantitatively measure the presence of electroactive products (H_2O_2 in this case). Additionally, the flow cell can operate in generation or generation/collection mode, wherein the operating principle is the same as in the case of a rotating ring disk electrode.[48,49]

The following electrocatalysis experiments were obtained using a flowing, aqueous solution of O_2-saturated, 0.10 M $HClO_4$. The GE was a PPF modified with the electrocatalyst, while the CE was a quartz slide coated with a ∼100 nm-thick Pt film. The potential of the GE was scanned from 0.85 to −0.36 V, while the potential of the CE was held constant at 1.34 V to oxidize H_2O_2 formed at the upstream GE.

Figure 6a is a Levich plot showing the relationship between the current observed at the GE (i_{GE}) at −0.16 V (mass transport-limited region) and the cube root of the flow rate (representative ORR linear sweep voltammograms are provided in the Supporting Information: Figure S18 ($TiO_{1.9}$) and Figure S19 ($TiO_{2.0}$)).

The Levich equation predicts a linear relationship between i_{GE} and (flow rate)$^{1/3}$ if the Lévêque approximation holds in the system.[50,51] This linear relationship is borne out for all four electrode modifications considered herein: PPF/TiO_x(60)/G6-NH_2(Au_{147}) and PPF/TiO_x(60)/Au_{147} (x = 1.9 and 2.0);

Next, we evaluated n_{eff} for each of the four electrode modifications using eq 2.[52]

$$n_{eff} = 4\left(\frac{Ni_{GE}}{Ni_{GE} + i_{CE}}\right) \quad (2)$$

Here, N is collection coefficient (57 ± 10%)[2], and i_{ce} is current at the CE. Figure 6b shows the relationship between n_{eff} and (flow rate)$^{1/3}$ with the GE potential set at −0.16 V. For the PPF/TiO_x(60)/G6-NH_2(Au_{147}) electrode, n_{eff} is ∼2.5 (blue and black). This means that in the absence of direct interactions between AuNPs and TiO_x (x = 1.9 and 2.0) supports, the ORR results primarily in H_2O_2 as the product. In contrast, after removal of the dendrimer, n_{eff} is ∼3.6 and ∼3.5 on PPF/$TiO_{1.9}$(60)/Au_{147} (red) and PPF/$TiO_{2.0}$(60)/Au_{147} (green), respectively, indicating that in the presence of direct interactions between AuNPs and TiO_x supports, H_2O is the dominant product.

The key conclusion of this part of the study is that there are clear differences in the ORR pathway when AuNPs interact

https://dx.doi.org/10.1021/acs.jpcc.0c02754
J. Phys. Chem. C 2020, 124, 10045−10056

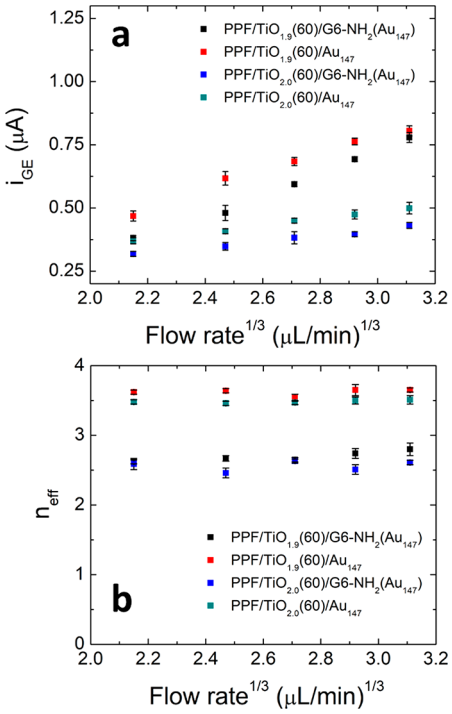

Figure 6. (a) Plot showing the relationship between i_{GE} and (flow rate)$^{1/3}$ for the GE compositions shown in the figure legend. (b) Plot showing the relationship between n_{eff} and (flow rate)$^{1/3}$ for the GE compositions shown in the legend. For both parts a and b, the GE was scanned from 0.85 to −0.36 V at 0.050 V/s in O_2-saturated 0.10 M $HClO_4$ and the Pt CE was held at 1.35 V. For each flow rate, i_{GE} and i_{CE} were extracted at −0.16 V, which is in the mass transport-limited region. The error bars represent the standard deviation of the mean value for three independently prepared electrodes.

directly with the TiO_x films compared to the absence of such interactions. In other words, the TiO_x/Au interaction results in both a shift in the onset potential for the ORR and a shift in the product distribution. Additionally, the experiments represented in Figure 6 took ∼3 h to complete, indicating that the system is stable on this time scale.

Electronic Interactions between TiO_x (x = 1.9 and 2.0) Support and AuNPs. DFT calculations presented earlier suggested that the enhanced ORR activity on TiO_x/Au electrocatalysts is observed due to partial charge transfer from the oxygen vacancies in TiO_x to the supported AuNPs. This in turn leads to a decrease in the OH* binding energy on Au. We next aim to corroborate this theoretical hypothesis by investigating the electronic states of AuNPs and TiO_x films using experimental methods. Specifically, XPS was used to determine the BEs of Au 4f and Ti 2p before and after UV/O_3 treatment of the PPF/TiO_x(60)/G6-NH_2(Au_{147}) supports. If the theoretical prediction is correct, and charge transfer occurs from the oxygen vacancies in TiO_x to the supported AuNPs (during direct contact), then we should observe a shift for Au toward lower BEs and a corresponding shift in the opposite direction for Ti.

The black traces in Figure 7a,b show the Au 4f and Ti 2p regions of PPF/$TiO_{1.9}$(60)/G6-NH_2(Au_{147})-modified electrodes before UV/O_3 treatment. The two Au peaks are present at 84.36 eV (Au $4f_{7/2}$) and 88.03 eV (Au $4f_{5/2}$), which correspond to zerovalent Au.[3,23] Two peaks are also present for Ti: 458.84 eV (Ti $2p_{3/2}$) and 464.54 eV (Ti $2p_{1/2}$). These peak positions and their separation suggest the dominance of the Ti^{4+} oxidation state.[23,53,54]

Following XPS analysis, the same PPF/$TiO_{1.9}$(60)/G6-NH_2(Au_{147}) electrode was exposed to UV/O_3 to remove the dendrimer and place the AuNPs and the $TiO_{1.9}$ film into direct contact. To ensure that Au oxides, which could be generated

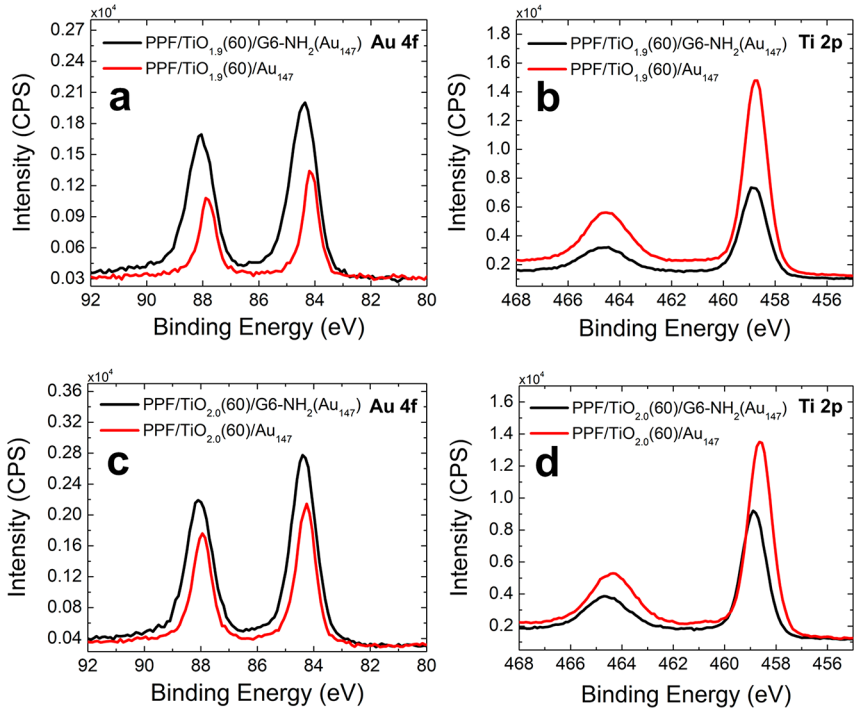

Figure 7. High-resolution XPS spectra in the Au 4f and Ti 2p regions for the indicated electrode configurations. XPS peaks were referenced to the position of the PPF C 1s peak at 284.50 eV.[23,24] The analysis was performed on using three independently prepared electrodes.

https://dx.doi.org/10.1021/acs.jpcc.0c02754
J. Phys. Chem. C 2020, 124, 10045−10056

by the UV/O_3 treatment, were removed, the supported NPs were electrochemically reduced back to metallic Au. The red spectra in Figure 7a,b correspond to these materials. In this case, the Au peaks occur at 84.15 eV (Au $4f_{7/2}$) and 87.82 eV (Au $4f_{5/2}$), which represent a shift of 0.21 ± 0.03 eV toward lower BE when the AuNPs and $TiO_{1.9}$ are in direct contact. This indicates an increased electron density on the AuNPs compared to when they are encapsulated within the dendrimers.

Curiously, the Ti peaks shift in the same direction as the Au peaks following UV/O_3 treatment. Specifically, there is a shift of 0.13 ± 0.04 eV toward lower BE for both Ti peaks when the AuNPs are in direct contact with $TiO_{1.9}$. This is surprising, because we would anticipate that if electron density increases on the AuNPs, then it should decrease on $TiO_{1.9}$. However, we observe the same trend for the stochiometric PPF/$TiO_{2.0}$(60)/G6-NH_2(Au_{147}) electrodes.

The black traces in Figure 7c,d show the Au 4f and Ti 2p regions of PPF/$TiO_{2.0}$(60)/G6-NH_2(Au_{147}) before UV/O_3 treatment. Both the Au 4f and Ti 2p peaks appear at the same positions as those for the substochiometric supports. The red traces in Figure 7c,d show the Au 4f and Ti 2p regions of PPF/$TiO_{2.0}$(60)/Au_{147}-electrodes after UV/O_3 and subsequent electrochemical reduction of oxides on the AuNPs. The data reveal a 0.11 ± 0.04 eV shift toward lower BE for Au 4f and a 0.21 ± 0.03 eV shift toward lower BE for Ti 2p when the AuNPs and $TiO_{2.0}$ films are in contact compared to those when they are separated.

The shape and separation of the Ti 2p peaks do not indicate an increased concentration of Ti^{3+} in the lattice structure of either oxidation state of TiO_x, and therefore the observed negative BE shift does not seem to be related to the reduction of TiO_x. A simultaneous shift toward lower BEs in both the Au 4f and Ti 2p peaks during direct contact has previously been attributed to formation of a Schottky barrier at the junction of AuNPs and TiO_x films,[55] but we have no direct evidence of this in our system. There are several other studies in the literature that also report charge transfer from TiO_2 to Au and simultaneous negative BEs shifts for both TiO_2 and Au.[53−58] Similar behavior has been observed for Pt and TiO_2 too.[59,60] In any case, the XPS evidence suggests that charge transfer does proceed from oxygen vacancies within TiO_x to AuNPs as predicted by DFT.

To further confirm our findings, we performed a set of control experiments, where XPS measurements were obtained for AuNPs in the absence and presence of direct contact with PPF electrodes (no TiO_x). As stated earlier, PPF is not known to affect the electronic state of supported metal NPs.[47] Figure S20 shows XPS spectra of PPF/G6-NH_2(Au_{147}) before and after dendrimer removal and electrochemical reduction of Au oxides. Importantly, in this case, the Au 4f lines are consistent with metallic Au, and they do not shift after removal of the dendrimer.

CONCLUSION

In summary, we have presented a model system for studying interactions between metal oxide supports, in this case TiO_x, and AuNPs. DFT calculations predicted that when AuNPs are in direct contact with TiO_x a significant, favorable shift in the onset potential for the ORR should be observed (compared to the case when AuNPs are isolated from the support). This is a consequence of electron donation into the supported AuNPs by oxygen vacancies. Experimental electrochemical and spectroscopic results confirm this prediction.

The results described here are fully consistent with our earlier findings of two different, but related, metal oxide/NP systems. Specifically, we showed that there is no change in the electrocatalytic activity of PtNPs for the ORR regardless of whether they are in contact with the nonreducible oxide Al_2O_3.[2] Additionally, as predicted by theory, a relatively large improvement in the onset potential of the ORR was observed when AuNPs were in contact with SnO_x.[3] The key point is that we have developed a highly reliable experimental model that provides a means for testing first-principles calculations for rather complex electrocatalytic systems. We plan to continue challenging the calculations by examining smaller AuNPs, other oxide supports, and different electrocatalytic reactions. The results of those experiments will be reported in due course.

ASSOCIATED CONTENT

Supporting Information

The Supporting Information is available free of charge at https://pubs.acs.org/doi/10.1021/acs.jpcc.0c02754.

Atomic structures; fabrication of pyrolyzed photoresist films; TEM micrographs and particle-size distributions; Gibbs free-energy diagram for AuNPs; surface Pourbaix diagram; X-ray diffraction data; Gibbs free energy diagram for TiO_2(110)/Au; Bader charge analysis; thickness analysis of ALD films; SEM images; stability test data; optical profilometry; high-resolution XPS spectra; ORR data (PDF)

AUTHOR INFORMATION

Corresponding Authors

Graeme Henkelman − *Department of Chemistry and Oden Institute for Computational Engineering and Science, The University of Texas at Austin, Austin, Texas 78712-1224, United States;* orcid.org/0000-0002-0336-7153; Email: henkelman@utexas.edu

Richard M. Crooks − *Department of Chemistry, Center for Electrochemistry, and Texas Materials Institute, The University of Texas at Austin, Austin, Texas 78712-1224, United States;* orcid.org/0000-0001-5186-4878; Email: crooks@cm.utexas.edu

Authors

Aigerim Galyamova − *Department of Chemistry and Center for Electrochemistry, The University of Texas at Austin, Austin, Texas 78712-1224, United States*

Kihyun Shin − *Department of Chemistry and Oden Institute for Computational Engineering and Science, The University of Texas at Austin, Austin, Texas 78712-1224, United States;* orcid.org/0000-0002-1748-8773

Complete contact information is available at: https://pubs.acs.org/10.1021/acs.jpcc.0c02754

Author Contributions

[$]These authors contributed equally.

Notes

The authors declare no competing financial interest.

https://dx.doi.org/10.1021/acs.jpcc.0c02754
J. Phys. Chem. C 2020, 124, 10045−10056

■ ACKNOWLEDGMENTS

We gratefully acknowledge support from the Chemical Sciences, Geosciences, and Biosciences Division, Office of Basic Energy Sciences, Office of Science, U.S. Department of Energy (Contract: DE-SC0010576). We thank the Robert A. Welch Foundation (RMC: Grant F-0032 and GH: Grant F-1841) for sustained support of our research. Computational resources were provided by the National Energy Research Scientific Computing Center and the Texas Advanced Computing Center. We also thank Texas Materials Institute for assistance with TiO_x thin film characterization.

■ REFERENCES

(1) Ostojic, N.; Thorpe, J. M.; Crooks, R. M. Electron Transfer Facilitated by Dendrimer-Encapsulated Pt Nanoparticles Across Ultrathin, Insulating Oxide Films. *J. Am. Chem. Soc.* **2016**, *138*, 6829−6837.

(2) Anderson, M. J.; Ostojic, N.; Crooks, R. M. Microelectrochemical Flow Cell for Studying Electrocatalytic Reactions on Oxide-Coated Electrodes. *Anal. Chem.* **2017**, *89*, 11027−11035.

(3) Ostojic, N.; Duan, Z.; Galyamova, A.; Henkelman, G.; Crooks, R. M. Electrocatalytic Study of the Oxygen Reduction Reaction at Gold Nanoparticles in the Absence and Presence of Interactions with SnO_x Supports. *J. Am. Chem. Soc.* **2018**, *140*, 13775−13785.

(4) Ostojic, N.; Crooks, R. M. Electrocatalytic Reduction of Oxygen on Platinum Nanoparticles in the Presence and Absence of Interactions with the Electrode Surface. *Langmuir* **2016**, *32*, 9727−9735.

(5) Zhao, M.; Sun, L.; Crooks, R. M. Preparation of Cu Nanoclusters Within Dendrimer Templates. *J. Am. Chem. Soc.* **1998**, *120*, 4877−4878.

(6) Myers, V. S.; Weir, M. G.; Carino, E. V.; Yancey, D. F.; Pande, S.; Crooks, R. M. Dendrimer-Encapsulated Nanoparticles: New Synthetic and Characterization Methods and Catalytic Applications. *Chem. Sci.* **2011**, *2*, 1632−1646.

(7) Bronstein, L. M.; Shifrina, Z. B. Dendrimers as Encapsulating, Stabilizing, or Directing Agents for Inorganic Nanoparticles. *Chem. Rev.* **2011**, *111*, 5301−5344.

(8) Lhenry, S.; Jalkh, J.; Leroux, Y. R.; Ruiz, J.; Ciganda, R.; Astruc, D.; Hapiot, P. Tunneling Dendrimers. Enhancing Charge Transport Through Insulating Layer Using Redox Molecular Objects. *J. Am. Chem. Soc.* **2014**, *136*, 17950−17953.

(9) Zhou, W. P.; Axnanda, S.; White, M. G.; Adzic, R. R.; Hrbek, J. Enhancement in Ethanol Electrooxidation by SnO_x Nanoislands Grown on Pt(111): Effect of Metal Oxide-Metal Interface Sites. *J. Phys. Chem. C* **2011**, *115*, 6467−16473.

(10) Sasaki, K.; Zhang, L.; Adzic, R. R. Niobium Oxide-Supported Platinum Ultra-Low Amount Electrocatalysts for Oxygen Reduction. *Phys. Chem. Chem. Phys.* **2008**, *10*, 159−167.

(11) Kowal, A.; Li, M.; Shao, M.; Sasaki, K.; Vukmirovic, M. B.; Zhang, J.; Marinkovic, N. S.; Liu, P.; Frenkel, A. I.; Adzic, R. R. Ternary $Pt/Rh/SnO_2$ Electrocatalysts for Oxidizing Ethanol to CO_2. *Nat. Mater.* **2009**, *8*, 325−330.

(12) Li, J.; Zhou, H.; Zhuo, H.; Wei, Z.; Zhuang, G.; Zhong, X.; Deng, S.; Li, X.; Wang, J. Oxygen Vacancies on TiO_2 Promoted the Activity and Stability of Supported Pd Nanoparticles for the Oxygen Reduction Reaction. *J. Mater. Chem. A* **2018**, *6*, 2264−2272.

(13) Ranganathan, S.; McCreery, R. L. Electroanalytical Performance of Carbon Films with Near-Atomic Flatness. *Anal. Chem.* **2001**, *73*, 893−900.

(14) Perdew, J. P.; Wang, Y. Accurate and Simple Analytic Representation of the Electron-Gas Correlation Energy. *Phys. Rev. B: Condens. Matter Mater. Phys.* **1992**, *45*, 13244−13249.

(15) Duan, Z.; Henkelman, G. CO Oxidation at the Au/TiO_2 Boundary: The Role of the Au/TiSc Site. *ACS Catal.* **2015**, *5*, 1589−1595.

(16) Duan, Z.; Henkelman, G. Calculations of CO Oxidation Over a Au/TiO2 Catalyst: A Study of Active Sites, Catalyst Deactivation, and Moisture Effects. *ACS Catal.* **2018**, *8*, 1376−1383.

(17) Hansen, H. A.; Rossmeisl, J.; Nørskov, J. K. Surface Pourbaix Diagrams and Oxygen Reduction Activity of Pt, Ag and Ni(111) Surfaces Studied by DFT. *Phys. Chem. Chem. Phys.* **2008**, *10*, 3722−3730.

(18) Nørskov, J. K.; Rossmeisl, J.; Logadottir, A.; Lindqvist, L.; Kitchin, J. R.; Bligaard, T.; Jónsson, H. Origin of the Overpotential for Oxygen Reduction at a Fuel-Cell Cathode. *J. Phys. Chem. B* **2004**, *108*, 17886−17892.

(19) Man, I. C.; Su, H.-Y.; Calle-Vallejo, F.; Hansen, H. A.; Martínez, J. I.; Inoglu, N. G.; Kitchin, J.; Jaramillo, T. F.; Nørskov, J. K.; Rossmeisl, J. Universality in Oxygen Evolution Electrocatalysis on Oxide Surfaces. *ChemCatChem* **2011**, *3*, 1159−1165.

(20) Peterson, A. A.; Abild-Pedersen, F.; Studt, F.; Rossmeisl, J.; Nørskov, J. K. How Copper Catalyzes the Electroreduction of Carbon Dioxide into Hydrocarbon Fuels. *Energy Environ. Sci.* **2010**, *3*, 1311−1315.

(21) Liu, S.; White, M. G.; Liu, P. Mechanism of Oxygen Reduction Reaction on Pt(111) in Alkaline Solution: Importance of Chemisorbed Water on Surface. *J. Phys. Chem. C* **2016**, *120*, 15288−15298.

(22) Gröhn, F.; Bauer, B. J.; Akpalu, Y. A.; Jackson, C. L.; Amis, E. J. Dendrimer Templates for the Formation of Gold Nanoclusters. *Macromolecules* **2000**, *33*, 6042−6050.

(23) *NIST X-Ray Photoelectron Spectroscopy Database*, Version 4.1, National Institute of Standards and Technology: Gaithersburg, MD, http://srdata.nist.gov/xps/.

(24) Loussaert, J. A.; Fosdick, S. E.; Crooks, R. M. Electrochemical Properties of Metal-Oxide-Coated Carbon Electrodes Prepared by Atomic Layer Deposition. *Langmuir* **2014**, *30*, 13707−13715.

(25) Candela, G. A.; Chandler-Horowitz, D.; Marchiando, J. F.; Novotny, D. B.; Belzer, B. J.; Croarkin, M. C. *Standard Reference Materials: Preparation and Certification of SRM-2530, Ellipsometric Parameters Δ and Ψ and Derived Thickness and Refractive Index of a Silicon Dioxide Layer on Silicon*; U.S. Government Printing Office: Washington, DC, 1988.

(26) Siefke, T.; Kroker, S.; Pfeiffer, K.; Puffky, O.; Dietrich, K.; Franta, D.; Ohlídal, I.; Szeghalmi, A.; Kley, E.-B.; Tünnermann, A. Materials Pushing the Application Limits of Wire Grid Polarizers Further into the Deep Ultraviolet Spectral Range. *Adv. Opt. Mater.* **2016**, *4*, 1780−1786.

(27) Duan, Z.; Li, Y.; Timoshenko, J.; Chill, S. T.; Anderson, R. M.; Yancey, D. F.; Frenkel, A. I.; Crooks, R. M.; Henkelman, G. A Combined Theoretical and Experimental EXAFS Study of the Structure and Dynamics of Au_{147} Nanoparticles. *Catal. Sci. Technol.* **2016**, *6*, 6879−6885.

(28) Stephens, I. E. L.; Bondarenko, A. S.; Grønbjerg, U.; Rossmeisl, J.; Chorkendorff, I. Understanding the Electrocatalysis of Oxygen Reduction on Platinum and Its Alloys. *Energy Environ. Sci.* **2012**, *5*, 6744−6762.

(29) Rossmeisl, J.; Karlberg, G. S.; Jaramillo, T.; Nørskov, J. K. Steady State Oxygen Reduction and Cyclic Voltammetry. *Faraday Discuss.* **2009**, *140*, 337−46 discussion 417−37..

(30) Pham, H. H.; Wang, L.-W. Oxygen Vacancy and Hole Conduction Amorphous TiO_2. *Phys. Chem. Chem. Phys.* **2015**, *17*, 541−550.

(31) Tang, W.; Sanville, E.; Henkelman, G. A Grid-Based Bader Analysis Algorithm Without Lattice Bias. *J. Phys.: Condens. Matter* **2009**, *21*, 084204.

(32) Sanville, E.; Kenny, S. D.; Smith, R.; Henkelman, G. Improved Grid-Based Algorithm for Bader Charge Allocation. *J. Comput. Chem.* **2007**, *28*, 899−908.

(33) Henkelman, G.; Arnaldsson, A.; Jónsson, H. A Fast and Robust Algorithm for Bader Decomposition of Charge Density. *Comput. Mater. Sci.* **2006**, *36*, 354−360.

(34) Yu, M.; Trinkle, D. R. Accurate and Efficient Algorithm for Bader Charge Integration. *J. Chem. Phys.* **2011**, *134*, 64111.

https://dx.doi.org/10.1021/acs.jpcc.0c02754
J. Phys. Chem. C 2020, 124, 10045−10056

(35) Niemelä, J.-P.; Marin, G.; Karppinen, M. Titanium Dioxide Thin Films by Atomic Layer Deposition: a Review. *Semicond. Sci. Technol.* **2017**, *32*, 1−43.
(36) Chazalviel, J.-N.; Allongue, P. On the Origin of the Efficient Nanoparticle Mediated Electron Transfer Across a Self-Assembled Monolayer. *J. Am. Chem. Soc.* **2011**, *133*, 762−764.
(37) Kissling, G. P.; Miles, D. O.; Fermín, D. J. Electrochemical Charge Transfer Mediated by Metal Nanoparticles and Quantum Dots. *Phys. Chem. Chem. Phys.* **2011**, *13*, 21175.
(38) Gooding, J. J.; Alam, M. T.; Barfidokht, A.; Carter, L. Nanoparticle Mediated Electron Transfer Across Organic Layers: from Current Understanding to Applications. *J. Braz. Chem. Soc.* **2013**, *25*, 418−426.
(39) Hill, C. M.; Kim, J.; Bard, A. J. Electrochemistry at a Metal Nanoparticle on a Tunneling Film: A Steady-State Model of Current Densities at a Tunneling Ultramicroelectrode. *J. Am. Chem. Soc.* **2015**, *137*, 11321−11326.
(40) Sun, L.; Crooks, R. M. Imaging of Defects Contained Within n-Alkylthiol Monolayers by Combination of Underpotential Deposition and Scanning Tunneling Microscopy: Kinetics of Self-Assembly. *J. Electrochem. Soc.* **1991**, *138*, L23−L25.
(41) Kaipio, M.; et al. Atomic Layer Deposition, Characterization, and Growth Mechanistic Studies of TiO_2 Thin Films. *Langmuir* **2014**, *30*, 7395−7404.
(42) Szindler, M.; Szindler, M. M.; Boryło, P.; Jung, T. Structure and Optical Properties of TiO_2 Thin Films Deposited by ALD Method. *Open Physics* **2017**, *15*, 1067−1071.
(43) Tao, Q.; Overhage, K.; Jursich, G.; Takoudis, C. On the Initial Growth of Atomic Layer Deposited TiO_2 Films on Silicon and Copper Surfaces. *Thin Solid Films* **2012**, *520*, 6752−6756.
(44) Beamson, G.; Briggs, D. *High Resolution XPS of Organic Polymers: The Scienta ESCA300 Database*; Wiley: New York, NY, 1992.
(45) Ramanathan, S.; Chi, D.; McIntyre, P. C.; Wetteland, C. J.; Tesmer, J. R. Ultraviolet-Ozone Oxidation of Metal Films. *J. Electrochem. Soc.* **2003**, *150*, F110−F115.
(46) Torresi, R. M.; Cámara, O. R.; Pauli, C. P. de; Giordano, M. C. Hydrogen Evolution Reaction on Anodic Titanium Oxide Films. *Electrochim. Acta* **1987**, *32*, 1291−1301.
(47) Cuenya, B. R. Synthesis and Catalytic Properties of Metal Nanoparticles: Size, Shape, Support, Composition, and Oxidation State Effects. *Thin Solid Films* **2010**, *518*, 3127−3150.
(48) Aoki, K.; Tokuda, K.; Matsuda, H. Hydrodynamic Voltammetry at Channel Electrodes. *J. Electroanal. Chem. Interfacial Electrochem.* **1977**, *79*, 49−78.
(49) Barnes, E. O.; Lewis, G. E. M.; Dale, S. E. C.; Marken, F.; Compton, R. G. Generator-Collector Double Electrode Systems: a Review. *Analyst* **2012**, *137*, 1068−1081.
(50) Levich, V. G. *Physicochemical Hydrodynamics*, 2nd ed., Prentice-Hall, Englewood Cliffs, NJ, 1962.
(51) Compton, R. G.; Unwin, P. R. Channel and Tubular Electrodes. *J. Electroanal. Chem. Interfacial Electrochem.* **1986**, *205*, 1−20.
(52) Antoine, O.; Durand, R. RRDE Study of Oxygen Reduction on Pt Nanoparticles Inside Nafion®: H_2O_2 Production in PEMFC Cathode Conditions. *J. Appl. Electrochem.* **2000**, *30*, 839−844.
(53) Atuchin, V. V.; Kesler, V. G.; Pervukhina, N. V.; Zhang, Z. Ti 2p and O 1s Core Levels and Chemical Bonding in Titanium-Bearing Oxides. *J. Electron Spectrosc. Relat. Phenom.* **2006**, *152*, 18−24.
(54) Biesinger, M. C.; Lau, L. W. M.; Gerson, A. R.; Smart, R. St. C Resolving Surface Chemical States in XPS Analysis of First Row Transition Metals, Oxides and Hydroxides: Sc, Ti, V, Cu and Zn. *Appl. Surf. Sci.* **2010**, *257*, 887−898.
(55) Zhang, Z.; Yates, J. T. Band Bending in Semiconductors: Chemical and Physical Consequences at Surfaces and Interfaces. *Chem. Rev.* **2012**, *112*, 5520−5551.
(56) Chen, M. S.; Goodman, D. W. Interaction of Au with Titania: the Role of Reduced Ti. *Top. Catal.* **2007**, *44*, 41−47.
(57) Kruse, N.; Chenakin, S. XPS Characterization of Au/TiO_2 Catalysts: Binding Energy Assessment and Irradiation Effects. *Appl. Catal., A* **2011**, *391*, 367−376.
(58) Minato, T.; Susaki, T.; Shiraki, S.; Kato, H. S.; Kawai, M.; Aika, K.-i. Investigation of the Electronic Interaction Between TiO_2(110) Surfaces and Au Clusters by PES and STM. *Surf. Sci.* **2004**, *566*, 1012−1017.
(59) Chen, B. H.; White, J. M. Properties of Platinum Supported on Oxides of Titanium. *J. Phys. Chem.* **1982**, *86*, 3534−3541.
(60) Lewera, A.; Timperman, L.; Roguska, A.; Alonso-Vante, N. Metal−Support Interactions Between Nanosized Pt and Metal Oxides (WO_3 and TiO_2) Studied Using X-ray Photoelectron Spectroscopy. *J. Phys. Chem. C* **2011**, *115*, 20153−20159.

https://dx.doi.org/10.1021/acs.jpcc.0c02754
J. Phys. Chem. C 2020, 124, 10045−10056